Radar-sounding characterization of the subglacial groundwater table beneath Hiawatha Glacier, Greenland

Jonathan T. Bessette[1,2], Dustin M. Schroeder[2,3], Thomas M. Jordan[2,4], and Joseph A. MacGregor[5]

[1]Department of Mechanical and Aerospace Engineering, University at Buffalo, Buffalo, NY, USA
[2]Department of Geophysics, Stanford University, Stanford, CA, USA
[3]Department of Electrical Engineering, Stanford University, Stanford, CA, USA
[4]School of Geographical Sciences, University of Bristol, Bristol, UK
[5]Cryospheric Sciences Laboratory, NASA Goddard Space Flight Center, Greenbelt, Maryland, USA

Key Points:

- Radiometric and hydrologic analysis of radar-sounding data is consistent with a reflection from a subglacial groundwater table
- Dual radiometric constraints indicate a layer of either debris-laden ice or fractured bedrock above the subglacial groundwater table
- This first detection of a subglacial groundwater table was enabled by favorable local geology, thin ice and the wide bandwidth radar system

Corresponding author: J. Bessette, `jbessett@buffalo.edu`

Abstract

Radar-sounding surveys associated with the discovery of a large impact crater beneath Hiawatha Glacier, Greenland, revealed bright, flat subglacial reflections hypothesized to originate from a subglacial groundwater table. We test this hypothesis using radiometric and hydrologic analysis of those radar data. The dielectric loss between the reflection from the top of the basal layer and subglacial reflection and their reflectivity difference represent dual constraints upon the complex permittivity of the basal material. Either ice-cemented debris or fractured, well-drained bedrock explain the basal layer's radiometric properties. The subglacial reflector's geometry is parallel to isopotential hydraulic head contours, located 7.5–15.3 m below the interface, and 11 ± 7 dB brighter than the ice–basal layer reflection. We conclude that this subglacial reflection is a groundwater table and that its detection was enabled by the wide bandwidth of the radar system and unusual geologic setting, suggesting a path for future direct radar detection of subglacial groundwater elsewhere.

Plain Language Summary

Recent radar-sounding of the Hiawatha Glacier, which overlies a large impact crater, also found an unusually flat, bright surface about ten meters beneath the bottom of the ice. This surface was suspected to be the groundwater table, which has never been directly detected beneath an ice sheet, but it was not studied in detail. We used two three-layer geologic models to test this hypothesis using the strength of the radar returns. We found that the layer between the ice bottom and this lower surface is likely either debris-laden ice or fractured, well-drained bedrock. This surface's shape and brightness is also consistent with a groundwater table, because it follows expected patterns of water pressure. Our results confirm the detection of a groundwater table beneath Hiawatha Glacier and show the potential for future radar surveys to further probe subglacial groundwater systems.

1 Introduction

Recent airborne radar-sounding surveys revealed a 31-km-wide impact crater beneath Hiawatha Glacier, part of the northwestern Greenland Ice Sheet (Kjær et al., 2018). These radar data were collected with a new ultrawideband (UWB) radar sounder that revealed the glacier's bed topography and internal structure in unprecedented detail (Wang et al., 2016; Yan et al., 2017). Within these data, Kjær et al. (2018) also identified a distinct reflection *beneath* the ice–bed interface that was unusually flat and specular, which they hypothesized to be the groundwater table. However, this observation has yet to be confirmed by radiometric or hydrologic analyses, and the intervening material sandwiched between the glacier and this reflection was not characterized.

The unique geologic setting of a subglacial complex impact crater could be partly responsible for this reflection. While the deglaciated region immediately adjacent to Hiawatha Glacier (Inglefield Land) is composed of highly metamorphosed Paleoproterozoic rock (Kjær et al., 2018), unconsolidated impact breccias are expected to be widespread within the crater floor surrounding the central uplift (Osinski & Pierazzo, 2013). Debris-rich ice is observed outcropping along the base of ice cliffs along the western margin of Hiawatha Glacier, and Kjær et al. (2018) hypothesized that basal material is being actively entrained within Hiawatha Glacier, based on the UWB radar sounding data. A possible second large subglacial impact crater has also been identified in Greenland (MacGregor et al., 2019), but no comparable subglacial reflection was reported there, although the ice is thicker and that structure is likely older.

Radar sounders are widely deployed to study subglacial and englacial water bodies (e.g., Wright & Siegert, 2012; Chu et al., 2018; Oswald et al., 2018; Jordan et al., 2018; Kendrick et al., 2018). This method often succeeds because the complex permittivity contrast between ice and water is large and because such bodies are often specular reflectors (e.g., Schroeder et al., 2015). Subglacial lakes are now regularly found beneath the Antarctica and Greenland ice sheets and inform our understanding of their subglacial hydrology (Wright & Siegert, 2012; Livingstone et al., 2019). Groundwater sources are an important component of glacier hydrology; they can drive water into till, elevate porewater pressures, reduce shear strength and significantly influence ice-sheet dynamics (Boulton et al., 1995; Gooch et al., 2016; Key & Siegfried, 2017; Siegert et al., 2018). Relatively few studies have reported detecting the subglacial groundwater table (modeling: Christoffersen et al, 2014; airborne transient electromagnetics: Mikucki et al., 2015) despite ground-penetrating radar surveys being well-established as a method for identifying groundwater in deglaciated environments (e.g., A. Neal, 2004; Woodward & Burke, 2007).

Radar-sounder designs range from ground-based impulse and frequency-modulated continuous-wave systems to multi-channel chirped airborne systems (Li et al., 2019). The UWB chirped radar system developed by the Center for Remote Sensing Ice Sheets and deployed by Kjær et al. (2018) is a relatively new version of the Multi-channel Coherent Radar Sounder (MCoRDS v5), characterized by a much larger bandwidth than previous versions, weaker sidelobes and a higher signal-to-noise ratio (SNR) (Rodrguez-Morales et al., 2013; Wang et al., 2016). The technical advances of MCoRDS v5 raise the possibility that its capabilities alone are what enabled the detection of the hypothesized subglacial groundwater table.

A reflection from a subglacial groundwater table ought to posses a radiometric signature distinct from off-nadir bed reflections, because the dielectric contrast that induces the reflection should be due to the contrast between unsaturated and saturated sediment, rather than between ice and more typical subglacial interfaces (marine sediment or bedrock). This reflection's subglacial depth should also be consistent with the predicted hydrology of groundwater flow through such systems. If the interface is indeed a water table, then it should be conformal to isopotential contours of hydraulic head (Wright et al., 2008; Flowers, 2015; Rutishauser et al., 2018). Here we test the hypothesis that the subglacial reflection at Hiawatha Glacier is indeed that of a groundwater table using both radiometric and hydrologic analyses. These tests inform an assessment of the cause of this reflection, prospects of its detectability elsewhere and provide a framework for future investigations of subglacial groundwater systems beneath glaciers and ice sheets.

2 Data and methods

The MCoRDS v5 data used in this study were collected in May 2016 (Kjær et al., 2018). The radar system is described in detail by Wang et al. (2016) and consists of three eight-element arrays, operating between 150–520 MHz at a 10-kHz pulse repetition frequency. These arrays were mounted on the Alfred Wegener Institute's Polar 6, a Basler BT-67 aircraft. After pulse compression and synthetic aperture processing, the data have a vertical (range) resolution of 0.5 m and an along-track (azimuth) resolution of 15 m. Figure 1 shows the four flight tracks and radargrams from this survey where the putative groundwater table was detected. The peak power of the putative groundwater-table reflection was extracted using a local depth window that was selected manually to bound this reflection. This depth window was also used to re-track some regions where the original ice–basal layer peak power picks corresponded with the hypothesized groundwater table.

2.1 Radiometric analysis

Our radiometric analysis aims to test whether the received power from the ice–basal layer and hypothesized basal layer–groundwater interface, along with the dielectric loss within the intervening basal layer, are consistent with a subglacial groundwater table. We assume that this system can be represented by a three-layer dielectric model, where the relative complex permittivity, $\tilde{\epsilon} = \epsilon' - j\epsilon''$ is uniform within each layer, where $j^2 = -1$ and $\tan\delta = \epsilon''/\epsilon'$ is the loss tangent (dielectric loss). Two different models for the basal layer are explored in parallel, and in each case the basal layer is described by a three-component mixture. We show below that the combination of reflectivity difference between the ice–basal layer and subglacial reflections and $\tan\delta$ within the basal layer provide dual constraints upon $\tilde{\epsilon}_b$.

For our first model, the top layer is polar ice with an assumed permittivity $\tilde{\epsilon}_{ice} = 3.15(1-j0.0062)$ expressed in the form $\tilde{\epsilon} = \epsilon'(1-j\tan\delta)$ (Fujita et al., 2000; Peters et al., 2005). The middle layer sandwiched between the ice–basal layer interface and the putative groundwater table has an unknown permittivity $\tilde{\epsilon}_b$ and is assumed to be a mixture of granitic sand, groundwater-saturated till and ice (with initially unknown volume fractions). The bottom layer(groundwater table) is modeled using the dielectric properties of thawed, groundwater-saturated granitic till $\tilde{\epsilon}_{gwt} = 25(1-j0.0118)$ (Christianson et al., 2016). These assumed layer compositions were selected *a posteriori* by testing a range of plausible subglacial permittivity values to maximize overlap between the dual constraints.We note that the dielectric contrast between the middle layer and the putative groundwater table is so great that our conclusions are not significantly affected by the plausible range of permittivity values for the middle layer.

The second model again includes a top layer of polar ice $\tilde{\epsilon}_{ice}$ and an unknown middle layer, but differs in assuming the bottom layer is a groundwater aquifer in porous or fractured granitic rock (rather than an unsorted till) with higher water content and thus higher permittivity ($\tilde{\epsilon}_{gw}$). In this case, the middle basal layer is assumed to be a mixture of fractured bedrock, water and air (rather than ice).

These two distinct models effectively test whether detection of the subglacial reflection is due to a thermal transition from frozen to thawed material (model 1), or due to a hydraulic transition from drained to saturated bedrock (model 2). Only their differences in the assumed composition of the bottom layer affect the resulting mixture ratios for the sandwiched basal layer. We consider these two cases to be the most plausible, with the primary goal of testing for the existence of the groundwater table rather than robustly identifying nature of the middle layer. For simplicity, the following sections use equations with subscripts and descriptions for model 1 only, but the analysis for model 2 is the same except using groundwater *gw* instead of groundwater-saturated till *gwt*.

The difference in received power between the basal layer–groundwater till (*b–gwt*) and the ice–basal layer (*ice–b*) reflectors is given by

$$\Delta[P] = \Delta[R] - [L_b], \tag{1}$$

where $\Delta[P] = [P_{b-gwt}] - [P_{ice-b}]$, $\Delta[R] = [R_{b-gwt}] - [R_{ice-b}]$ is the reflectivity difference between the basal layer–groundwater and the ice–basal layer reflections, $[L_b]$ is the dielectric attenuation within the basal layer material, and the notation $[X] = 10\log_{10} X$ is used for power in decibels. For this relation, birefringence loss and the radar system performance cancel out (Fujita et al., 2006; Matsuoka et al., 2012; Haynes, 2020).VHF birefringence within subglacial materials has not been reported so we neglect this possible confounding factor (Jordan et al., 2020). Given the small traveltime differences and plausible range of permittivities, suggesting a basal layer ∼10 m thick, the difference in geometric spreading loss between the ice–basal layer interface and groundwater interface is negligible and also ignored. To assess the potential effect of interface roughness upon reflection scattering loss and how it might impact interpretation of Δ[R], we compared the spread of the reflectivity distributions for the ice-basal layer interface and the basal layer-groundwater interface (see supplement) (Jordan et al., 2018; Grima et al., 2019).

Spatial variation in the thickness of the basal layer between the ice–basal layer interface and the putative groundwater table can be further exploited to estimate the mean dielectric attenuation rate within this layer (Campbell et al., 2008). This regression assumes that (linear) power decays exponentially with travel time t (equivalent to layer thickness for uniform ϵ_b'), resulting in a linear relationship between $\Delta[P]$ and t. This method also assumes that $\tan\delta_b$ is uniform, that volume scattering within the layer is negligible, and that roughness-induced scattering losses and $[R_{b-gwt}]$ are uncorrelated with t. By neglecting volume scattering within this middle layer , our estimate of water content in the basal layer is a conservative upper bound. $[L_b]$ is obtained for each along-track sample using the regression slope $(-\Delta[P]/\Delta t)$ and $\Delta[R]$ is obtained using Eq. (1). The loss tangent of the sandwiched basal layer is thus

$$\tan\delta_b = \sqrt{\left\{2\Big(\frac{\lambda}{40\pi c\log_{10}(e)}\frac{\Delta\,[P]}{\Delta t}\Big)^2+1\right\}^2-1}, \tag{2}$$

where λ is the radar wavelength in the vacuum (0.9 m), c is its speed in the vacuum and Δt is the two-way travel time (Campbell et al., 2008). This approach differs from the typical procedure to estimate englacial attenuation rates, where power is regressed against ice thickness for an assumed value of ϵ_{ice}' (Jacobel et al., 2009). The rationale for our approach, which was originally applied to the subsurface of Mars (Campbell et al., 2008), is that we cannot assume a value for ϵ_b' *a priori.*

The derived values of $\Delta[R]$ and $\tan\delta_b$ provide two independent constraints upon $\tilde{\epsilon}_b$ and hence its composition. To relate these constraints to $\tilde{\epsilon}_b$, we consider a three-component mixture of granite(considering a range of granitic sand to rock permittivities), ice, and groundwater-saturated till using a power-law mixing model of the form

$$\tilde{\epsilon}_{\mathrm{b}}^{\frac{1}{\gamma}} = \phi_{\mathrm{gran}}\tilde{\epsilon}_{\mathrm{gran}}^{\frac{1}{\gamma}} + \phi_{\mathrm{ice}}\tilde{\epsilon}_{\mathrm{ice}}^{\frac{1}{\gamma}} + \phi_{\mathrm{gwt}}\tilde{\epsilon}_{\mathrm{gwt}}^{\frac{1}{\gamma}}, \tag{3}$$

where $\tilde{\epsilon}_{\mathrm{gran}}$ is the complex permittivity of granite and ϕ_{gran}, ϕ_{ice}, ϕ_{gwt} are the fractional volumes of granite, ice and groundwater-saturated till, respectively (Wilhelms, 2005; Nerozzi & Holt, 2019). We assume γ=3 following Looyenga (1965) and a range of values for $\tilde{\epsilon}_{\mathrm{gran}}$ between $5(1{-}j6.8{\times}10^{-5})$ and $9(1{-}j0.068)$, with a mean value of $7(1{-}j0.034)$. These values were determined by converting electrical conductivity σ values for granite from between $10^{-5}-10^{-2}$ S m^{-1} (Bogorodsky et al., 1985) and considering a real permittivity range of 5 to 9 (Martinez & Barnes, 2001; Nerozzi & Holt, 2019), i.e. $\tilde{\epsilon}_{\mathrm{gran}} = \sigma_{gran}/(2\pi f\epsilon_{gran}'\epsilon_0)$ where f is the radar center frequency (335 MHz), ϵ_0 is the permittivity of the vacuum and $\epsilon_{gran}' = 5$ to 9. Expected values of $\Delta[R]$ and $\tan\delta_b$ were modeled using Eq. (3), assuming a specular Fresnel reflection for $\Delta[R]$, and evaluated for all possible fractional combinations of ϕ_{gran}, ϕ_{ice} and ϕ_{gwt} to produce a ternary diagram for each constraint.

2.2 Hydraulic analysis

Hydraulic head is a measure of liquid potential and its spatial pattern determines where groundwater flows (Freeze & Cherry, 1979). Here, we apply a traditional Darcian approach of evaluating the aquifers. We assume flow in one direction and a homogeneous aquifer in both models. For model 1, the total potential at the potentiometric surface (the elevation of the water table) is evaluated assuming the groundwater till aquifer is confined and partially driven by pressure from the top and middle layers (frozen basal layer and the overlying ice sheet). Model 2 considers flow through fractures dominated by gravity. While flow through such fractures is not well described by a simple Darcian model, for our purposes these simple hydraulic models enable the examination of the range of depths and shapes of the groundwater potential compared to the groundwater echo, rather than robustly modeling or supporting either of the two hydraulic scenarios.

To determine isopotential contours of hydraulic equilibrium, we calculate the hydraulic head as a function of elevation head and pressure head (neglecting velocity head) as

$$\Phi_1 = \rho_{gwt} g z_{gwt} + \rho_{ice} g (z_{surface} - z_b) + \rho_b g (z_b - z_{gwt}), \tag{4}$$

$$\Phi_2 = \rho_{gw} g z_{gw}, \tag{5}$$

where z is elevation, ρ is density and g is the acceleration due to Earth's gravity (Shreve, 1972; Rutishauser et al., 2018). Because the basal layer is thin (∼10 m), uncertainty in the density of the basal layer does not significantly affect the hydraulic head calculation and is neglected. We assume the basal layer density is comparable to granite (ρ_b = 2700 kg m^{-3}) used in prior studies of northwest Greenland and note that granitic sand at lower densities would produce similar results (Corbett et al., 2015; Vermassen et al., 2019). The density of groundwater-saturated till (ρ_{gwt}) and groundwater (ρ_{gw}) are both assumed to be 997 kg m^{-3}assuming the till will not flow (see supplement). To bound these two end members, both possibilities are shown in Figure 2.

2.3 Radar system analysis

We evaluate the performance parameters of MCoRDS v5 against those of other commonly deployed radar sounders to address whether MCoRDS v5 itself is responsible for the detection of a subglacial reflection. The characteristic bandwidths, center frequency, pulse length and windowing techniques are incorporated to generate and compare the sidelobe patterns of HiCARS (Peters et al., 2007), MCoRDS v3 (Shi et al., 2010) and MCoRDS v5 (see Table S1 for radar-system parameters used). This comparison tests whether the observed subglacial reflections are likely to be "visible", or stronger than the sidelobes from basal layer echoes.

3 Results

For our radiometric analysis, the four profiles where the subglacial reflection was detected were initially analyzed separately (Fig. 1). Best-fit loss tangents range between 0.0102 to 0.0128 (Fig. 2). The reflectivity difference between the ice–basal layer and basal layer–groundwater reflection, $\Delta[R]$, and hydraulic head are shown for each track section in Figure 2. The mean reflectivity difference ($\Delta[R]$) for all four profiles is 11.1 ± 6.8 dB, accounting for both the standard deviation of each segment and the propagated error in $[L_b]$ from the regression slope. The four reflectivity distributions all satisfy Lilliefors and Jarque-Bera tests for normality, and their mean spread (one standard deviation about $\Delta[R]$) is 6.0 dB.

To estimate the subglacial material composition, we first used the arithmetic mean to combined the individual profile-mean estimates of $\tan\delta_b$ and $\Delta[R]$, yielding $\tan\delta_b = 0.0115 \pm 0.0013$ and $\Delta[R] = 11.1 \pm 6.8$ dB. The regions of the ternary diagrams consistent with these estimates are shown in Fig. 3. The upper and lower bounds for the volume fractions consider the intersection of the outlined regions in Fig. 3b-c and Fig. 3e-f, which account for the full ranges of uncertainty in $\tan\delta_b$, ΔR and possible complex permittivity values of granite and groundwater till.

The first hypothesized model (Fig. 3a) results in material volume fractions of $\phi_{gwt} = 16 \pm 9\%$, $\phi_{ice} = 74 \pm 10\%$, $\phi_{gran} = 10 \pm 7\%$. Substituting these volume fractions into

Eq. (3), we derive $\tilde{\epsilon}_b = 4.67(1-j0.007) \pm 2.99(1-j0.001)$. Using the estimates for ϵ_b' and the mean travel times (Fig. 2a-d), the mean thickness of the basal layer between the ice and groundwater table, averaged over the four sections, is 13 ± 4.7 m. Both this loss and reflectivity analysis indicate the presence of a debris-laden basal ice layer above a groundwater table. The second hypothesized model (Fig. 3d) resulted in material volume fractions of $\phi_{gw} = 1 \pm 1\%$, $\phi_{ice} = 39 \pm 23\%$, $\phi_{gran} = 60 \pm 23\%$, bedrock permittivity of $\tilde{\epsilon}_b = 5.39(1-j0.009) \pm 5.15(1-j0.045)$, and indicate the presence of drained, fractured bedrock 9.8 ± 2.8 m thick. While the two models differ, both are consistent with a groundwater table located ∼10 m below overlying material of either (1) ice-cemented debris or (2) drained, fractured bedrock.

Equipotential hydraulic head lines were compared against the groundwater interfaces for all segments, and the interfaces often followed isocontours (Fig. 2i-l). Thus, the interfaces are qualitatively consistent with a groundwater table in hydrologic equilibrium. The deviations from these isopotential lines appear to be related with deviations of the flight tracks from the local ice-flow direction, especially toward the northwestern margin of the ice sheet. The lateral extent of the groundwater system is ∼15 km^2.

Analysis of sidelobe patterns shows the potential of MCoRDS v5 and other systems to detect similar subglacial groundwater tables (Figure 4). MCoRDS v3 could plausibly detect nearly all Hiawatha subglacial groundwater reflections, but many would be on the edge of detectability for HiCARS due to its narrower bandwidth (15 MHz). This interpretation is favored because the subglacial groundwater table reflections only slightly exceed the sidelobes generated by basal layer echoes from these two systems. However, for MCoRDS v5 these subglacial reflections are consistently tens of decibels higher than the sidelobes. Therefore, the combination of high SNR and wide bandwidth – resulting in faster sidelobe fall-off – is likely a significant factor in explaining why the subglacial groundwater table was detected beneath a portion of Hiawatha Glacier. The lack of detection of the subglacial groundwater table in other regions of the crater could be because: 1. No groundwater table is present there; 2. The basal layer is insufficiently frozen or drained to permit substantial radio-wave penetration; 3. The groundwater table is not sufficiently contiguous to identify in the radargrams; or 4. The interface is too deep to be detected.

4 Discussion and conclusions

Both our radiometric and hydrologic analysis are consistent with the anomalous subglacial reflection originating from a groundwater table beneath either a well-drained or partially frozen basal layer within the Hiawatha impact crater floor. Our radiometric analysis shows the groundwater-table reflection is typically over 10 dB stronger than the overlying ice–basal layer reflection, strongly indicative of the presence of water-saturated material, i.e., a groundwater aquifer.

Our first hypothesized model (Fig. 3a) indicates that an ice-cemented debris layer lies above thawed, saturated groundwater till, consistent of a mixture of groundwater till, granite, and ice, with ratios of approximately 16%, 10%, and 74%, respectively. In this model, water can exist both above and below the aquitard of the frozen basal layer, and the low attenuation rate of the basal layer is the result of its thermal state, i.e., the pores are filled with ice rather than water. The underlying thawed layer might also be trapped by frozen layers above it, a feature observed in firn hydrology (Koenig et al., 2014; Chu et al., 2018). This layer could be liquid because it is confined and pressurized (Steinbrügge et al., 2020), due to refreezing, heat advected by subglacial water flow or higher salinity (Rutishauser et al., 2018).

Our second hypothesized model (Fig. 3d) indicates a basal layer of porous, well-drained rock above the groundwater table consisting of 1% groundwater, 60% granite, and 39% ice. In this case, the low-loss basal layer is the result of efficient vertical drainage rather than freezing. The impact should have produced a thick layer of impact breccia, which would be permeable and conducive to rapid subglacial drainage from the overlying glacier into a groundwater system, and this second model indirectly assumes that this layer is still present. Thus, the unique detection of this subglacial groundwater table could be in part due to the uniqueness of its geologic setting.

The radar profiles where the groundwater table was detected are found close to each other, within the northwestern section of the crater (Kjær et al., 2018). A map of the ice–basal layer reflectivity from the 2016 survey indicates increasing relative reflectivity from the southeastern corner of the crater toward its northwestern corner (Fig. S3). Our hydrologic analyses are also consistent with this drainage pattern, in that deviations of the observed groundwater table depth from equipotential hydraulic contours show a pattern of decreasing pressure gradient toward the northwest. This pattern suggests that groundwater is indeed flowing through the crater towards the ice-sheet margin in the same direction indicated by Kjær et al. (2018). Further investigation into character and flow of the subglacial and groundwater hydrology of the Hiawatha Glacier region of Greenland will require more sophisticated modeling, such as considering variations in hydraulic conductivity and intrinsic permeability.

As unusual as the geologic setting of Hiawatha Glacier may be, observation of its groundwater was also partly enabled by the large bandwidth and SNR of the MCoRDS v5 system. Additional surveys by similar wideband sounders over other sites with known or hypothesized groundwater, or surveys of Hiawatha Glacier region by other radar sounders could validate the potential for wider applications of this work. This conclusion raises the possibility that other subglacial groundwater systems could be mapped using wideband radar sounders, providing new insights into the poorly understood role of groundwater in the subglacial hydrology of Greenland, Antarctica and other glaciated regions (Key & Siegfried, 2017; Siegert et al., 2018; Williams et al., 2020).

Acknowledgments

We thank the Stanford Summer Undergraduate Research in Geoscience and Engineering Program and R. Culberg for making this work possible. DMS was supported, in part, by an NSF CAREER Award and by NASA grant NNX16AJ95G. TMJ acknowledges support from EU Horizons 2020 grant 747336-BRISRES-H2020-MSCA-IF-2016. Datasets used for this study are available through CReSIS (2016) and Morlighem et. al. (2017). Ternary plot code is courtesy of Ulrich Theune, Statoil's Research centre in Trondheim (Theune, 2020). Figure 1i was created with the Antarctic Mapping Tools (Greene et al., 2017).

References

Bogorodsky, V. V., Bentley, C. R., & Gudmandsen, P. E. (1985). *Radioglaciology* (Vol. 1). Dordrecht, Holland: D. Riedel.

Boulton, G., Caban, P., & Van Gijssel, K. (1995). Groundwater flow beneath ice sheets: Part ILarge scale patterns. *Quaternary Science Reviews*, *14*(6), 545–562. doi: https://doi.org/10.1016/0277-3791(95)00039-R

Campbell, B., Carter, L., Phillips, R., Plaut, J., Putzig, N., Safaeinili, A., … Orosei, R. (2008). SHARAD radar sounding of the Vastitas Borealis Formation in Amazonis Planitia. *Journal of Geophysical Research: Planets*, *113*(E12). doi: https://doi.org/10.1029/2008JE003177

Christianson, K., Jacobel, R. W., Horgan, H. J., Alley, R. B., Anandakrishnan, S., Holland, D. M., & DallaSanta, K. J. (2016). Basal conditions at the grounding zone of Whillans Ice Stream, West Antarctica, from ice-penetrating radar.

Journal of Geophysical Research: Earth Surface, *121*(11), 1954-1983. doi: https://doi.org/10.1002/2015JF003806

Christoffersen, P., Bougamont, M., Carter, S. P., Fricker, H. A., & Tulaczyk, S. (2014). Significant groundwater contribution to Antarctic ice streams hydrologic budget. *Geophysical Research Letters*, *41*(6), 2003–2010. doi: https://doi.org/10.1002/2014GL059250

Chu, W., Schroeder, D. M., & Siegfried, M. (2018). Retrieval of Englacial Firn Aquifer Thickness From Ice-Penetrating Radar Sounding in Southeastern Greenland. *Geophysical Research Letters*, *45*(21), 11–770. doi: https://doi.org/10.1029/2018GL079751

Corbett, L. B., Bierman, P. R., Lasher, G. E., & Rood, D. H. (2015). Landscape chronology and glacial history in Thule, northwest Greenland. *Quaternary Science Reviews*, *109*, 57–67. doi: https://doi.org/10.1016/j.quascirev.2014.11.019

CReSIS. (2016). 2016 greenland polar6 data. `https://data.cresis.ku.edu/data/rds/2016_Greenland_Polar6/`.

Flowers, G. E. (2015). Modelling water flow under glaciers and ice sheets. *Proceedings of the Royal Society A: Mathematical, Physical and Engineering Sciences*, *471*(2176). doi: https://doi.org/10.1098/rspa.2014.0907

Freeze, R. A., & Cherry, J. A. (1979). *Groundwater*. Englewood Cliffs, NJ: Prentice-hall.

Fujita, S., Maeno, H., & Matsuoka, K. (2006). Radio-wave depolarization and scattering within ice sheets: a matrix-based model to link radar and ice-core measurements and its application. *Journal of Glaciology*, *52*(178), 407–424. doi: https://doi.org/10.3189/172756506781828548

Fujita, S., Matsuoka, T., Ishida, T., Matsuoka, K., & Mae, S. (2000). A summary of the complex dielectric permittivity of ice in the megahertz range and its applications for radar sounding of polar ice sheets. In *Physics of ice core records* (pp. 185–212). Retrieved from `http://hdl.handle.net/2115/32469`

Gooch, B. T., Young, D. A., & Blankenship, D. D. (2016). Potential groundwater and heterogeneous heat source contributions to ice sheet dynamics in critical submarine basins of East Antarctica. *Geochemistry, Geophysics, Geosystems*, *17*(2), 395–409. doi: https://doi.org/10.1002/2015GC006117

Greene, C. A., Gwyther, D. E., & Blankenship, D. D. (2017). Antarctic mapping tools for MATLAB. *Computers & Geosciences*, *104*, 151–157. doi: https://doi.org/10.1016/j.cageo.2016.08.003

Grima, C., Koch, I., Greenbaum, J., Soderlund, K., Blankenship, D., Young, D., ... Fitzsimons, S. (2019). Surface and basal boundary conditions at the Southern McMurdo and Ross Ice Shelves, Antarctica. *Journal of Glaciology*, *65*(252), 675–688. doi: https://doi.org/10.1017/jog.2019.44

Grima, C., Schroeder, D. M., Blankenship, D. D., & Young, D. A. (2014). Planetary landing-zone reconnaissance using ice-penetrating radar data: Concept validation in antarctica. *Planetary and Space Science*, *103*, 191-204. doi: https://doi.org/10.1016/j.pss.2014.07.018

Haynes, M. S. (2020). Surface and subsurface radar equations for radar sounders. *Annals of Glaciology*, *61*(81), 135-142. doi: https://doi.org/10.1017/aog.2020.16

Jacobel, R. W., Welch, B. C., Osterhouse, D., Pettersson, R., & MacGregor, J. A. (2009). Spatial variation of radar-derived basal conditions on Kamb Ice Stream, West Antarctica. *Annals of Glaciology*, *50*(51), 1016. doi: https://doi.org/10.3189/172756409789097504

Jordan, T. M., Bamber, J. L., Williams, C. N., Paden, J. D., Siegert, M. J., Huybrechts, P., ... Gillet-Chaulet, F. (2016). An ice-sheet-wide framework for englacial attenuation from ice-penetrating radar data. *The Cryosphere*, *10*, 1547–1570. doi: https://doi.org/10.5194/tc-10-1547-2016

Jordan, T. M., Besson, D. Z., Kravchenko, I., Latif, U., Madison, B., Nokikov, A., & Shultz, A. (2020). Modeling ice birefringence and oblique radio wave propagation for neutrino detection at the south pole. *Annals of Glaciology*, *61*(81), 84–91.

Jordan, T. M., Williams, C. N., Schroeder, D. M., Martos, Y. M., Cooper, M. A., Siegert, M. J., … Bamber, J. L. (2018). A constraint upon the basal water distribution and thermal state of the Greenland Ice Sheet from radar bed echoes. *Cryosphere*, *12*, 2831-2854. doi: https://doi.org/10.5194/tc-12-2831-2018

Kendrick, A., Schroeder, D., Chu, W., Young, T. J., Christoffersen, P., Todd, J., … Lok, L. B. (2018). Surface meltwater impounded by seasonal englacial storage in West Greenland. *Geophysical Research Letters*, *45*(19), 10–474. doi: https://doi.org/10.1029/2018GL079787

Key, K., & Siegfried, M. R. (2017). The feasibility of imaging subglacial hydrology beneath ice streams with ground-based electromagnetics. *Journal of Glaciology*, *63*(241), 755771. doi: https://doi.org/10.1017/jog.2017.36

Kjær, K. H., Larsen, N. K., Binder, T., Bjørk, A. A., Eisen, O., Fahnestock, M. A., … MacGregor, J. A. (2018). A large impact crater beneath Hiawatha Glacier in northwest Greenland. *Science Advances*, *4*(11). doi: https://doi.org/10.1126/sciadv.aar8173

Koenig, L. S., Miège, C., Forster, R. R., & Brucker, L. (2014). Initial in situ measurements of perennial meltwater storage in the Greenland firn aquifer. *Geophysical Research Letters*, *41*(1), 81–85. doi: https://doi.org/10.1002/2013GL058083

Li, J., Rodrguez-Morales, F., Arnold, E., Leuschen, C., Paden, J., Shang, J., … Larsen, C. (2019). Airborne Snow Measurements Over Alaska Mountains and Glaciers With A Compact FMCW Radar. *IGARSS 2019 - 2019 IEEE International Geoscience and Remote Sensing Symposium*, 3906–3909. doi: https://doi.org/10.1109/IGARSS.2019.8900034

Livingstone, S. J., Sole, A. J., Storrar, R. D., Harrison, D., Ross, N., & Bowling, J. (2019). Brief communication: Subglacial lake drainage beneath Isunguata Sermia, West Greenland: Geomorphic and ice dynamic effects. *The Cryosphere*, *13*(10), 2789–2796. doi: https://doi.org/10.5194/tc-13-2789-2019

Looyenga, H. (1965). Dielectric constants of heterogeneous mixtures. *Physica*, *31*(3), 401-406. doi: https://doi.org/10.1016/0031-8914(65)90045-5

MacGregor, J. A., Bottke Jr, W. F., Fahnestock, M. A., Harbeck, J. P., Kjær, K. H., Paden, J. D., … Studinger, M. (2019). A possible second large subglacial impact crater in northwest Greenland. *Geophysical Research Letters*, *46*(3), 1496-1504. doi: https://doi.org/10.1029/2018GL078126

MacGregor, J. A., Li, J., Paden, J. D., Catania, G. A., Clow, G. D., Fahnestock, M. A., … Stillman, D. E. (2015). Radar attenuation and temperature within the Greenland Ice Sheet. *Journal of Geophysical Research: Earth Surface*, *120*(6), 983-1008. doi: https://doi.org/10.1002/2014JF003418

Martinez, A. L., & Barnes, A. P. (2001). Modeling dielectric-constant values of geologic materials. *Midcontinent Geoscience*, *247*, 1-16. Retrieved from `https://journals.ku.edu/mg/article/view/11831`

Matsuoka, K., MacGregor, J. A., & Pattyn, F. (2012). Predicting radar attenuation within the Antarctic ice sheet. *Earth and Planetary Science Letters*, *359*, 173–183. doi: https://doi.org/10.1016/j.epsl.2012.10.018

Mikucki, J. A., Auken, E., Tulaczyk, S., Virginia, R., Schamper, C., Sørensen, K., … Foley, N. (2015). Deep groundwater and potential subsurface habitats beneath an Antarctic dry valley. *Nature communications*, *6*(1), 1–9. doi: https://doi.org/10.1038/ncomms7831

Morlighem, M., Williams, C. N., Rignot, E., An, L., Arndt, J. E., Bamber, J. L., … Zinglerson, K. B. (2017). BedMachine v3: Complete bed topography and ocean bathymetry mapping of Greenland from multibeam echo sounding combined with mass conservation. *Geophysical research letters*, *44*(21), 11–051. doi: https://doi.org/10.1002/2017GL074954

Neal, A. (2004). Ground-penetrating radar and its use in sedimentology: principles, problems and progress. *Earth-science reviews*, *66*(3-4), 261–330. doi: https://doi.org/10.1016/j.earscirev.2004.01.004

Neal, C. S. (1982). Radio Echo Determination of Basal Roughness Characteristics on the Ross Ice Shelf. *Annals of Glaciology*, *3*, 216–221. doi: 10.1017/S0260305500002809

Nerozzi, S., & Holt, J. (2019). Buried ice and sand caps at the north pole of mars: revealing a record of climate change in the cavi unit with sharad. *Geophysical Research Letters*, *46*(13), 7278–7286. doi: https://doi.org/10.1029/2019GL082114

Osinski, G. R., & Pierazzo, E. (2013). *Impact cratering: Processes and products*. Oxford, United Kingdom: Blackwell Publishing Ltd.

Oswald, G. K., Rezvanbehbahani, S., & Stearns, L. A. (2018). Radar evidence of ponded subglacial water in Greenland. *Journal of Glaciology*, *64*(247), 711–729. doi: https://doi.org/10.1017/jog.2018.60

Peters, M. E., Blankenship, D. D., Carter, S. P., Kempf, S. D., Young, D. A., & Holt, J. W. (2007). Along-track focusing of airborne radar sounding data from West Antarctica for improving basal reflection analysis and layer detection. *IEEE Transactions on Geoscience and Remote Sensing*, *45*(9), 2725–2736. doi: https://doi.org/10.1109/TGRS.2007.897416

Peters, M. E., Blankenship, D. D., & Morse, D. L. (2005). Analysis techniques for coherent airborne radar sounding: Application to West Antarctic ice streams. *Journal of Geophysical Research: Solid Earth*, *110*(B6). doi: https://doi.org/10.1029/2004JB003222

Rodrguez-Morales, F., Gogineni, S., Leuschen, C. J., Paden, J. D., Li, J., Lewis, C. C., … others (2013). Advanced multifrequency radar instrumentation for polar research. *IEEE Transactions on Geoscience and Remote Sensing*, *52*(5), 2824–2842. doi: https://doi.org/10.1109/TGRS.2013.2266415

Rutishauser, A., Blankenship, D. D., Sharp, M., Skidmore, M. L., Greenbaum, J. S., Grima, C., … Young, D. A. (2018). Discovery of a hypersaline subglacial lake complex beneath Devon Ice Cap, Canadian Arctic. *Science advances*, *4*(4). doi: https://doi.org/10.1126/sciadv.aar4353

Schroeder, D. M., Blankenship, D. D., Raney, R. K., & Grima, C. (2015). Estimating subglacial water geometry using radar bed echo specularity: application to Thwaites Glacier, West Antarctica. *IEEE Geoscience and Remote Sensing Letters*, *12*(3), 443–447. doi: https://doi.org/10.1109/LGRS.2014.2337878

Shi, L., Allen, C. T., Ledford, J. R., Rodrguez-Morales, F., Blake, W. A., Panzer, B. G., … Gogineni, S. (2010). Multichannel coherent radar depth sounder for NASA operation ice bridge. In *2010 ieee international geoscience and remote sensing symposium* (pp. 1729–1732). doi: https://doi.org/10.1109/IGARSS.2010.5649518

Shreve, R. (1972). Movement of water in glaciers. *Journal of Glaciology*, *11*(62), 205–214. doi: https://doi.org/10.3189/S002214300002219X

Siegert, M. J., Kulessa, B., Bougamont, M., Christoffersen, P., Key, K., Andersen, K. R., … Smith, A. M. (2018). Antarctic subglacial groundwater: a concept paper on its measurement and potential influence on ice flow. *Geological Society, London, Special Publications*, *461*(1), 197–213. doi: https://doi.org/10.1144/SP461.8

Steinbrügge, G., Voigt, J., Wolfenbarger, N., Hamilton, C., Soderlund, K., Young, D., … Schroeder, D. (2020). Brine Migration and Impact-Induced Cryovolcanism on Europa. *Geophysical Research Letters*, *47*(21), e2020GL090797. doi: https://doi.org/10.1029/2020GL090797

Theune, U. (2020). Ternary plots. *MATLAB Central File Exchange*. Retrieved from `https://www.mathworks.com/matlabcentral/fileexchange/7210-ternary-plots`

Vermassen, F., Wangner, D. J., Dyke, L. M., Schmidt, S., Cordua, A. E., Kjær, K. H., … Andresen, C. S. (2019). Evaluating ice-rafted debris as a proxy for glacier calving in Upernavik Isfjord, NW Greenland. *Journal of Quaternary Science*, *34*(3), 258–267. doi: https://doi.org/10.1002/jqs.3095

Wang, Z., Gogineni, S., Rodrguez-Morales, F., Yan, J., Paden, J., Leuschen, C., … Braaten, D. (2016, March). Multichannel Wideband Synthetic Aperture Radar for Ice Sheet Remote Sensing: Development and the First Deployment in Antarctica. *IEEE Journal of Selected Topics in Applied Earth Observations and Remote Sensing*, *9*(3), 980-993. doi: 10.1109/JSTARS.2015.2403611

Wilhelms, F. (2005). Explaining the dielectric properties of firn as a density-and-conductivity mixed permittivity (DECOMP). *Geophysical Research Letters*, *32*(16). doi: https://doi.org/10.1029/2005GL022808

Williams, J. J., Gourmelen, N., & Nienow, P. (2020). Dynamic response of the Greenland ice sheet to recent cooling. *Scientific Reports*, *10*(1647). doi: https://doi.org/10.1038/s41598-020-58355-2

Woodward, J., & Burke, M. J. (2007). Applications of ground-penetrating radar to glacial and frozen materials. *Journal of Environmental & Engineering Geophysics*, *12*(1), 69–85. doi: https://doi.org/10.2113/JEEG12.1.69

Wright, A., & Siegert, M. (2012). A fourth inventory of Antarctic subglacial lakes. *Antarctic Science*, *24*(6), 659–664. doi: https://doi.org/10.1017/S095410201200048X

Wright, A., Siegert, M., Le Brocq, A., & Gore, D. (2008). High sensitivity of subglacial hydrological pathways in Antarctica to small ice-sheet changes. *Geophysical Research Letters*, *35*(17). doi: https://doi.org/10.1029/2008GL034937

Yan, J., Gomez-Garca Alvestegui, D., McDaniel, J. W., Li, Y., Gogineni, S., Rodrguez-Morales, F., … Leuschen, C. J. (2017). Ultrawideband FMCW Radar for Airborne Measurements of Snow Over Sea Ice and Land. *IEEE Transactions on Geoscience and Remote Sensing*, *55*(2), 834-843. doi: https://doi.org/10.1109/TGRS.2016.2616134

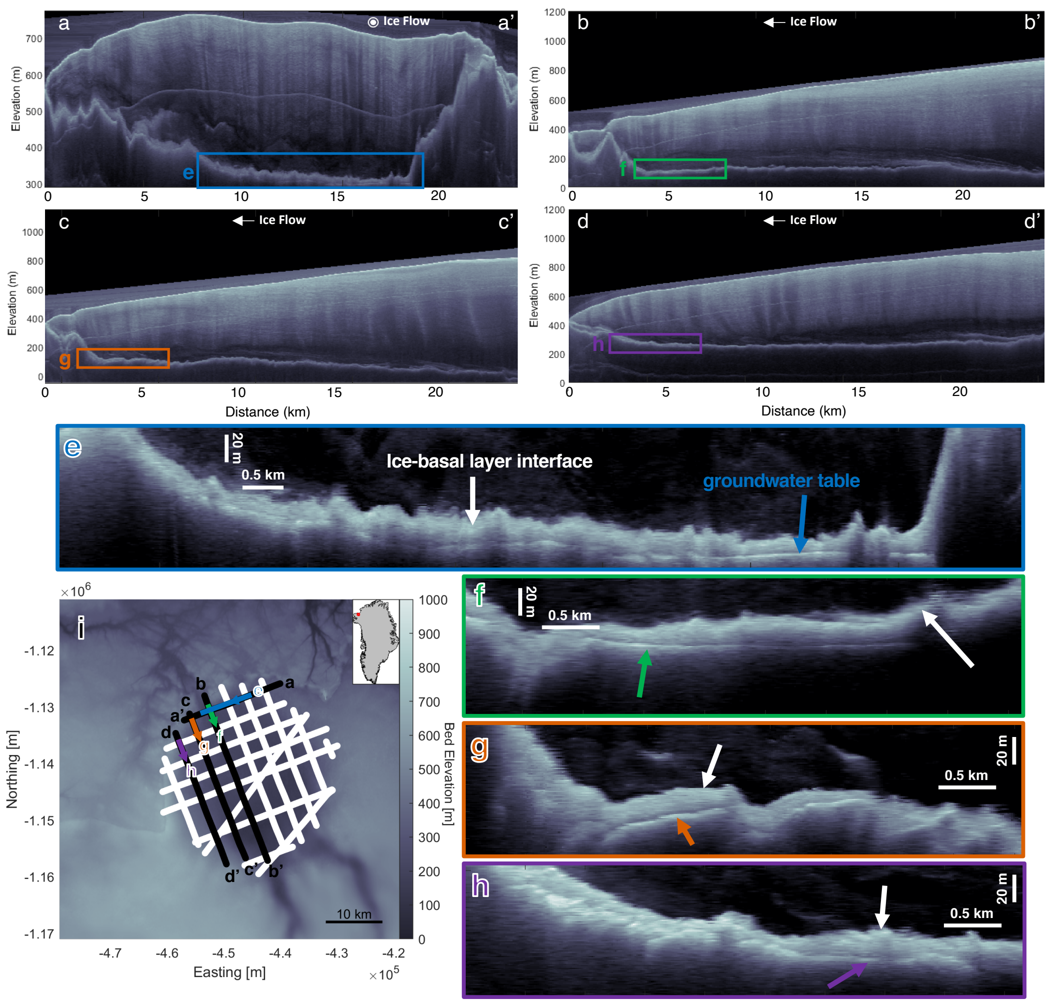

Figure 1. Radargrams from the 2016 Hiawatha Glacier survey and location of the hypothesized groundwater table. Panels a–d show full radargrams across the crater (20160517_03_008, 20160512_02_009, 20160516_02_006 and 20160512_02_007, respectively). Panels e–h are portions of a–d zoomed in on the hypothesized groundwater table. The vertical scale bar in e–h corresponds to the depth range in ice (assuming $\epsilon' = 3.15$), not sediment or rock. Panel i shows the bed topography (Morlighem et al., 2017) overlain by all the 2016 survey flights over the crater (white), with black segments (panels a-d) representing those with a potential subglacial groundwater table beneath a portion thereof (colors, panels e-h).

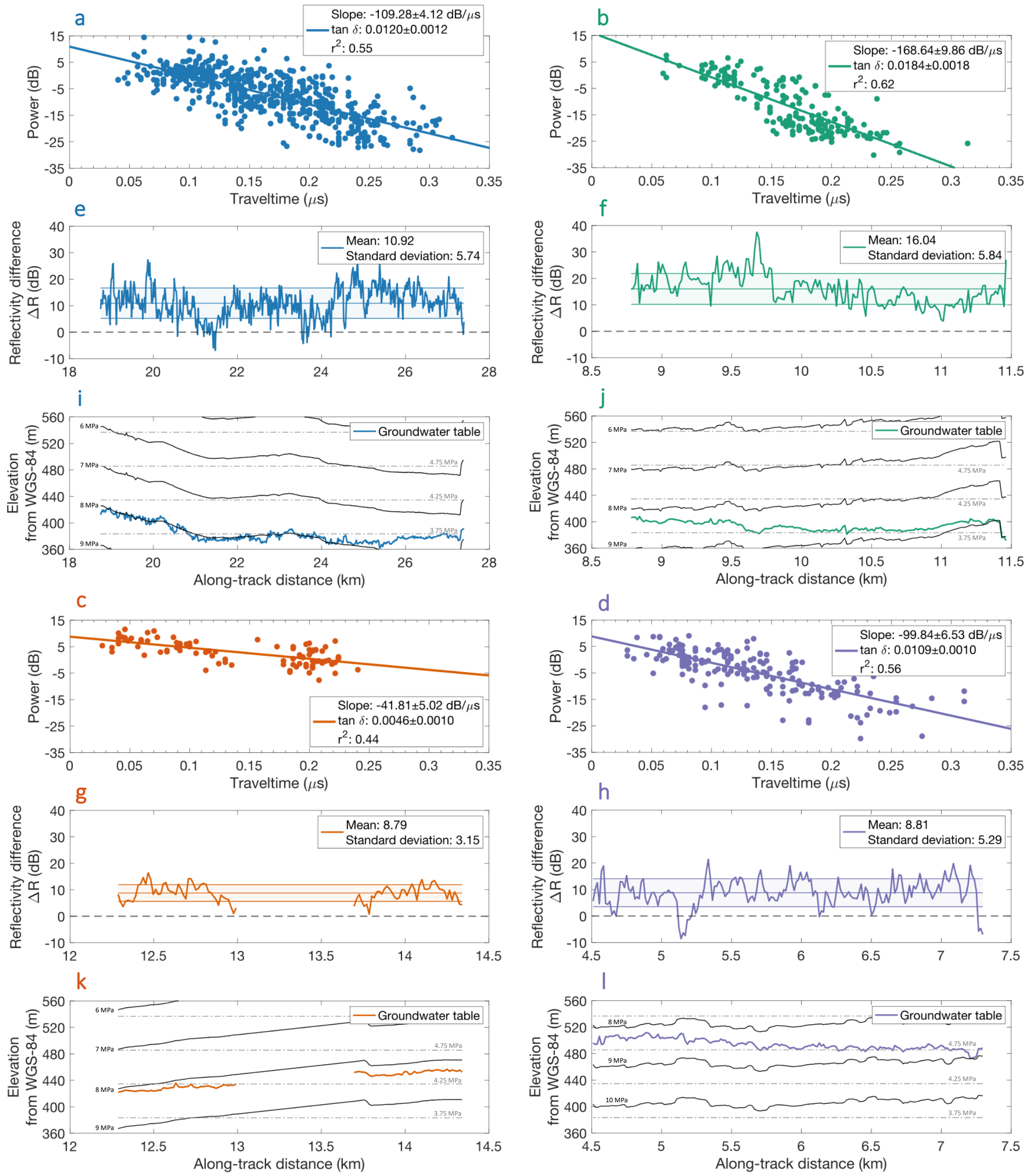

Figure 2. Radiometric data analysis for profiles shown in Fig. 1 e-h. Panels a-d show power loss in the basal layer material versus two-way travel time. The loss tangents are obtained from the regression slopes. Reflectivity difference between the basal layer–groundwater and ice–basal layer reflectors are shown in e-h and isopotential hydraulic head contours for the putative groundwater table in i-l.

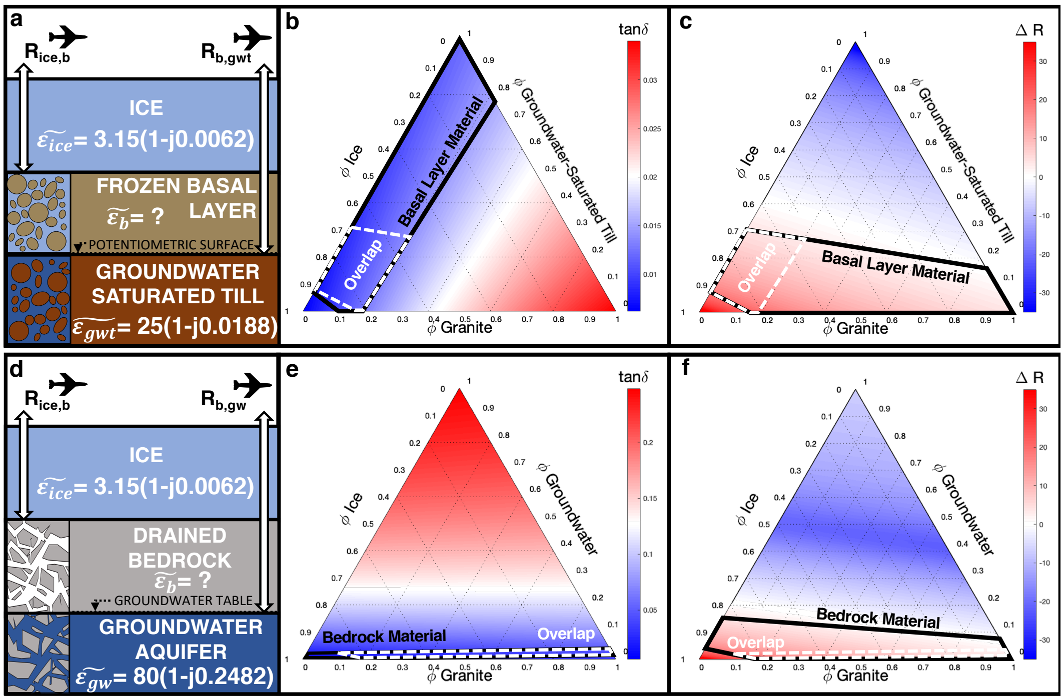

Figure 3. (a) Three-layer dielectric model of ice, a basal layer (constrained by the radiometric analysis), and groundwater-saturated till. (b) Ternary diagrams for $\tan\delta_b$ and (c) ΔR. The second row shows (d) a second hypothesized three-layer dielectric model of ice, bedrock, and groundwater. (e) Ternary diagrams for $\tan\delta_b$ and (f) ΔR with respect to the second model. Black outlined regions show most likely basal layer volume fractions, and dotted white outline showing the overlapping area of both the loss-tangent- and reflectivity-analysis probability regions. These ternary diagrams assume $\tilde{\epsilon}_{\rm gran} = 7(1 - j0.034)$, $\tilde{\epsilon}_{\rm gwt} = 25(1 - j0.0188)$ and $\tilde{\epsilon}_{\rm gw} = 80(1 - j0.2482)$ (Christianson et al., 2016), but the outlined regions encompass permittivity and conductivity ranges $5(1 - j6.8 \times 10^{-5}) < \tilde{\epsilon}_{\rm gran} < 9(1 - j0.068)$ (Bogorodsky et al., 1985; Martinez & Barnes, 2001; Nerozzi & Holt, 2019) and $20(1 - j0.005) < \tilde{\epsilon}_{\rm gwt} < 30(1 - j0.015)$ (Christianson et al., 2016).

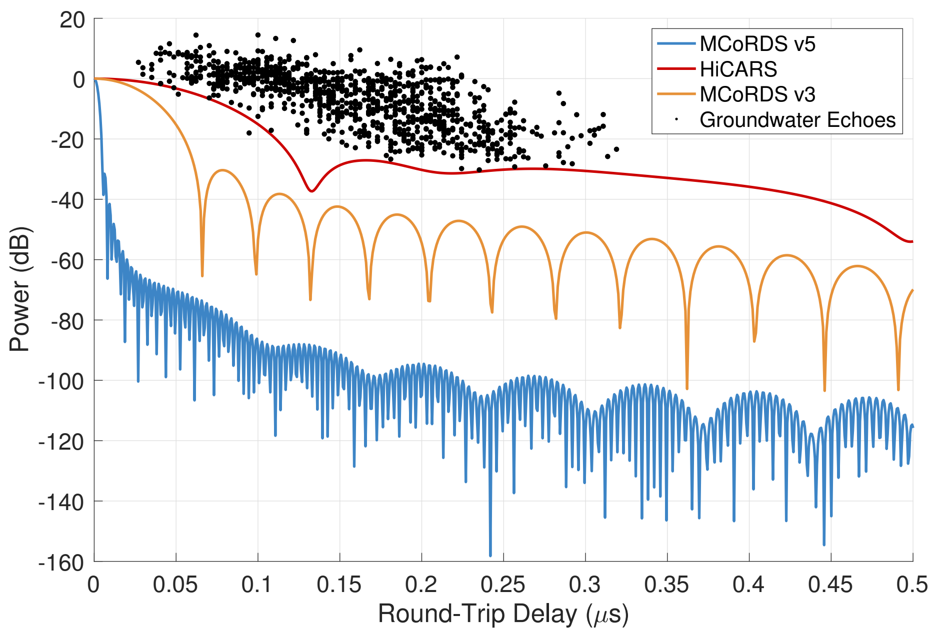

Figure 4. Antenna patterns for three radar systems (Table S1) compared against the putative groundwater echoes as a function of traveltime through the basal layer. The groundwater echoes are shown as in Fig. 2a-d. For each radar system, the potential detectability of the any echo increases with the difference in power between the echo and the radar system's antenna pattern, e.g., at a traveltime of 0.1 μs, the putative groundwater echoes are ∼70 dB above the noise floor of MCoRDS v5, but $<$ 15 dB above that of HiCARS.

Figure 1.

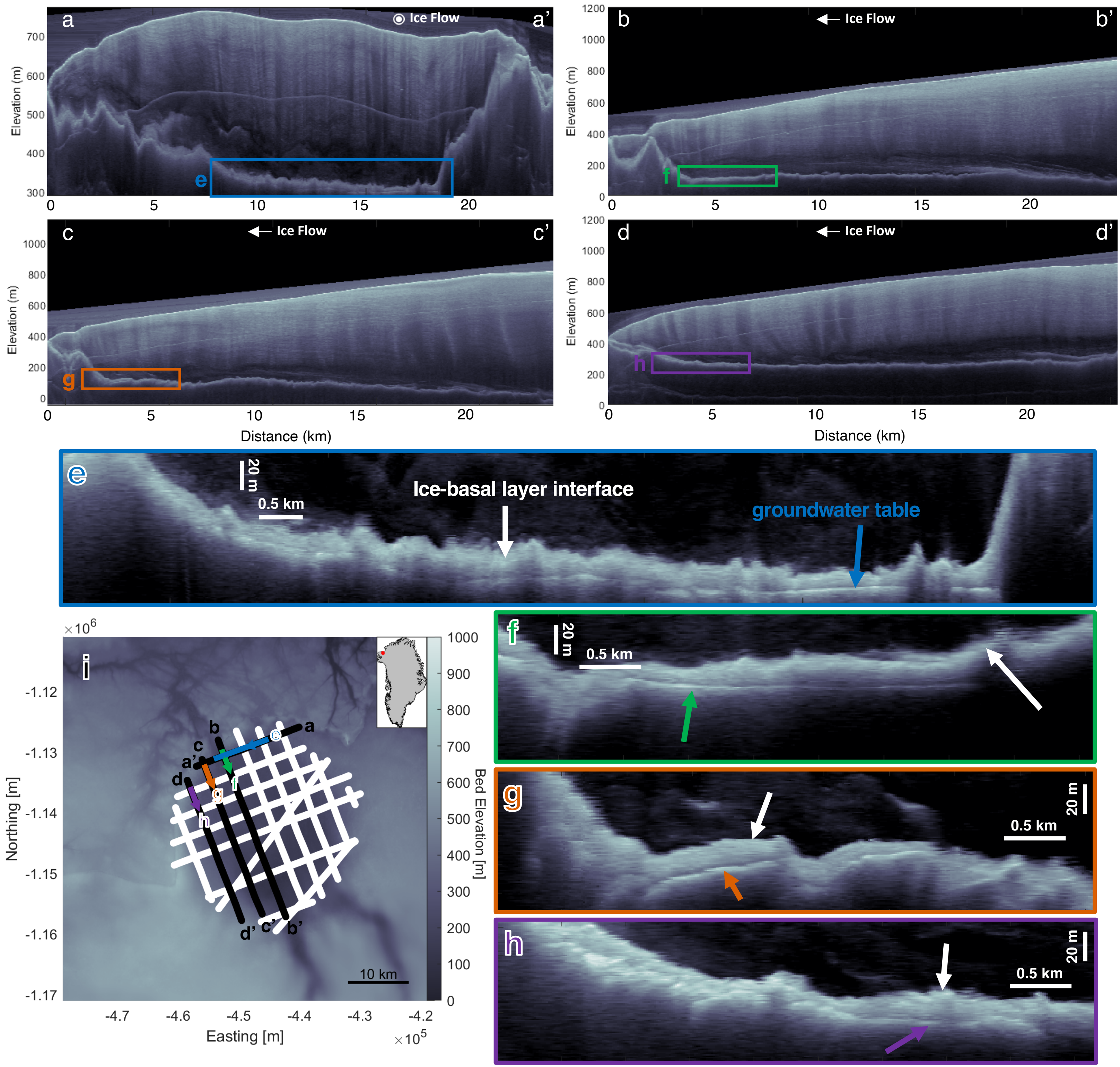

a
a'
Ice Flow
b
b'
c
c'
d
d'
Elevation (m)
Distance (km)
e
f
g
h
Ice-basal layer interface
groundwater table
20 m
0.5 km
i
Northing [m]
Easting [m]
Bed Elevation [m]
10 km

Figure 2.

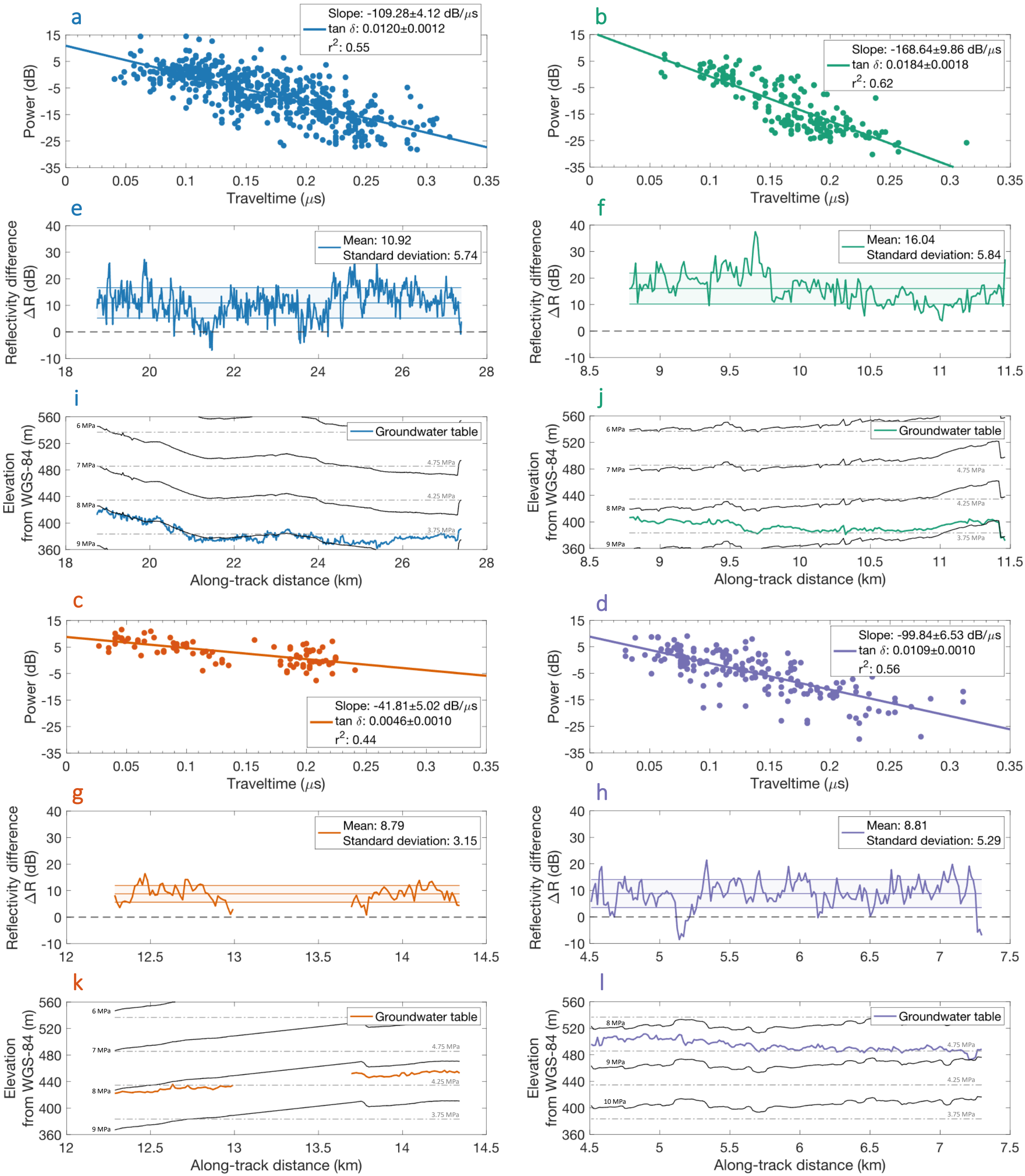

a
Slope: -109.28±4.12 dB/μs
tan δ: 0.0120±0.0012
r²: 0.55
Power (dB)
Traveltime (μs)
b
Slope: -168.64±9.86 dB/μs
tan δ: 0.0184±0.0018
r²: 0.62
e
Mean: 10.92
Standard deviation: 5.74
Reflectivity difference ΔR (dB)
f
Mean: 16.04
Standard deviation: 5.84
i
Groundwater table
Elevation from WGS-84 (m)
Along-track distance (km)
6 MPa
7 MPa
8 MPa
9 MPa
4.75 MPa
4.25 MPa
3.75 MPa
j
Groundwater table
c
Slope: -41.81±5.02 dB/μs
tan δ: 0.0046±0.0010
r²: 0.44
d
Slope: -99.84±6.53 dB/μs
tan δ: 0.0109±0.0010
r²: 0.56
g
Mean: 8.79
Standard deviation: 3.15
h
Mean: 8.81
Standard deviation: 5.29
k
Groundwater table
l
Groundwater table
10 MPa

Figure 3.

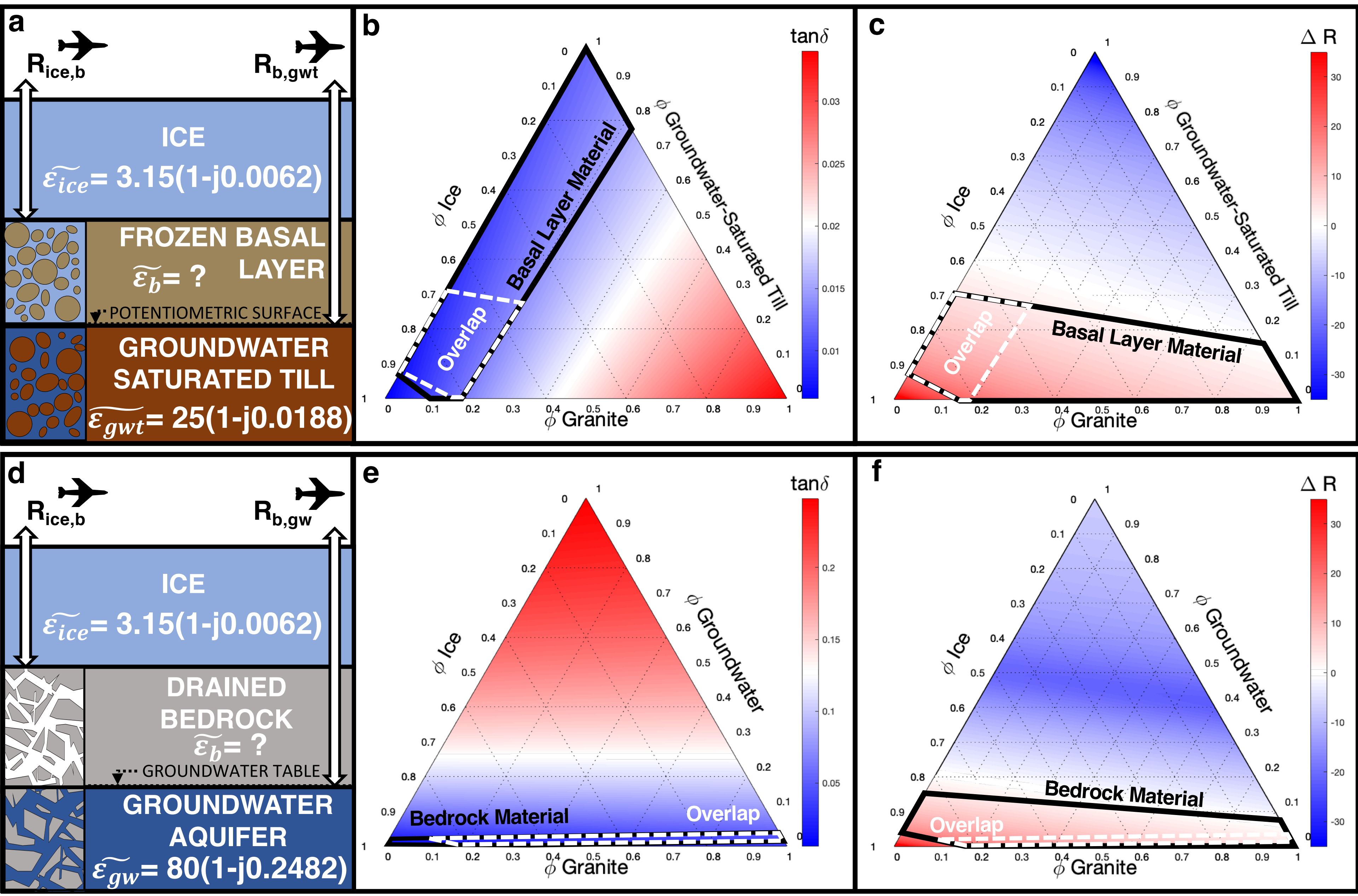

a
$R_{ice,b}$
$R_{b,gwt}$
ICE
$\widetilde{\varepsilon_{ice}}$= 3.15(1-j0.0062)
FROZEN BASAL LAYER
$\widetilde{\varepsilon_b}$= ?
POTENTIOMETRIC SURFACE
GROUNDWATER SATURATED TILL
$\widetilde{\varepsilon_{gwt}}$= 25(1-j0.0188)
b
tanδ
ϕ Ice
ϕ Groundwater-Saturated Till
ϕ Granite
Basal Layer Material
Overlap
c
Δ R
ϕ Ice
ϕ Groundwater-Saturated Till
ϕ Granite
Basal Layer Material
Overlap
d
$R_{ice,b}$
$R_{b,gw}$
ICE
$\widetilde{\varepsilon_{ice}}$= 3.15(1-j0.0062)
DRAINED BEDROCK
$\widetilde{\varepsilon_b}$= ?
GROUNDWATER TABLE
GROUNDWATER AQUIFER
$\widetilde{\varepsilon_{gw}}$= 80(1-j0.2482)
e
tanδ
ϕ Ice
ϕ Groundwater
ϕ Granite
Bedrock Material
Overlap
f
Δ R
ϕ Ice
ϕ Groundwater
ϕ Granite
Bedrock Material
Overlap

Figure 4.

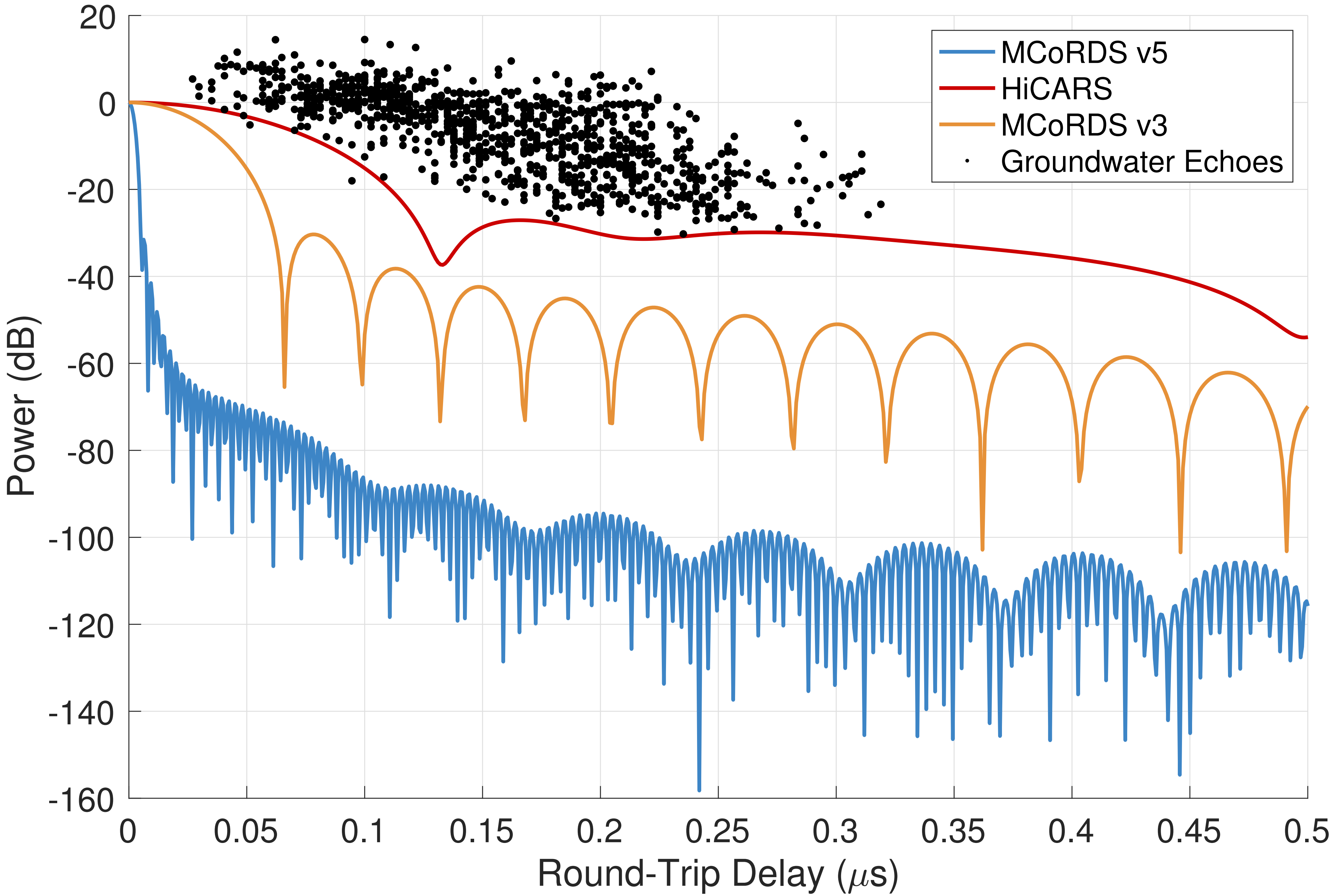

MCoRDS v5
HiCARS
MCoRDS v3
Groundwater Echoes
20
0
-20
-40
-60
-80
-100
-120
-140
-160
Power (dB)
0
0.05
0.1
0.15
0.2
0.25
0.3
0.35
0.4
0.45
0.5
Round-Trip Delay (μs)